Energy Materials

Supplementary Materials

Thermally induced urea-assisted porous precursor film for efficient planar inverted water-based perovskite solar cells

Zhongjun Dai[1,3,#], Mengnan Li[1,#], Yulin Zhang[2], Xiaofeng He[3,4], Zezhuan Jiang[3], Haimao Zhu[3], Yu Jiao[1], Jiasheng Chen[1], Yu Tan[3], Zirui Peng[3], Qunliang Song[3,*]

[1]School of Materials and Energy Engineering, Xichang University, Xichang 615013, Sichuan, China.
[2]Leshan West Silicon Materials Photovoltaic and New Energy Industry Technology Research Institute, Leshan 614000, Sichuan, China.
[3]Institute for Clean Energy and Advanced Materials, School of Materials and Energy, Southwest University, Chongqing 400715, China.
[4]Yibin Academy of Southwest University, Yibin 644000, Sichuan, China.

[*]**Correspondence to:** Prof. Qunliang Song, Institute for Clean Energy and Advanced Materials, School of Materials and Energy, Southwest University, Chongqing 400715, China. E-mail: qlsong@swu.edu.cn

ORCID: Qunliang Song (000000033797037X)

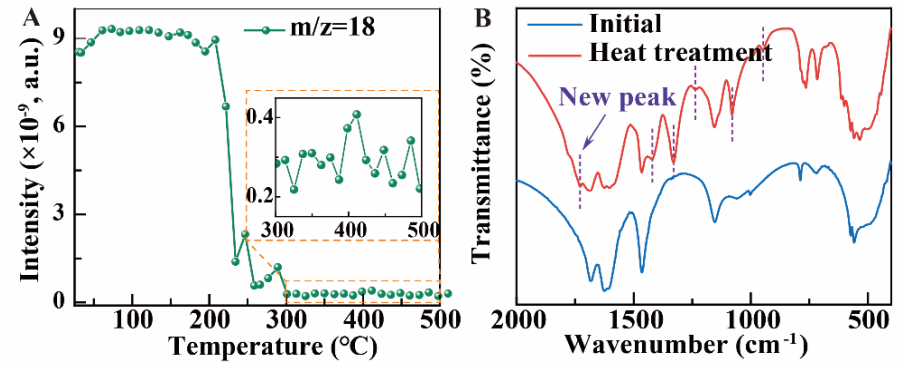

Supplementary Figure 1. (A) TG-MS profile of the m/z=18 signal assigned to H_2O during heating of urea under dry air. (B) FTIR spectra of urea before and after heat treatment.

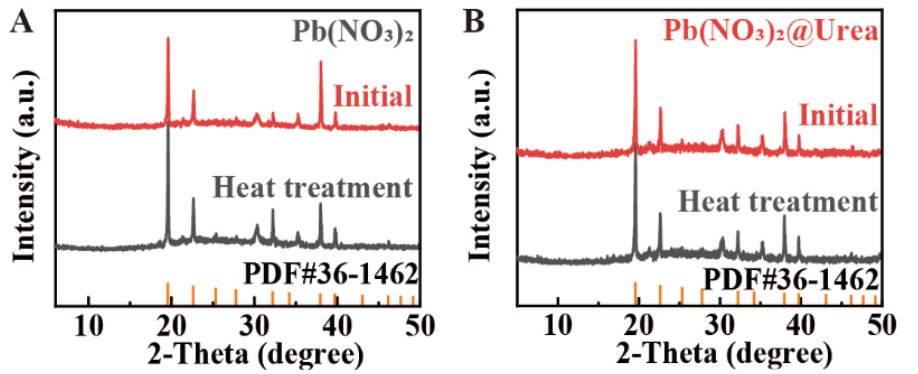

Supplementary Figure 2. The XRD of (A) $Pb(NO_3)_2$ and (B) $Pb(NO_3)_2$@urea precursor film before and after heat treatment.

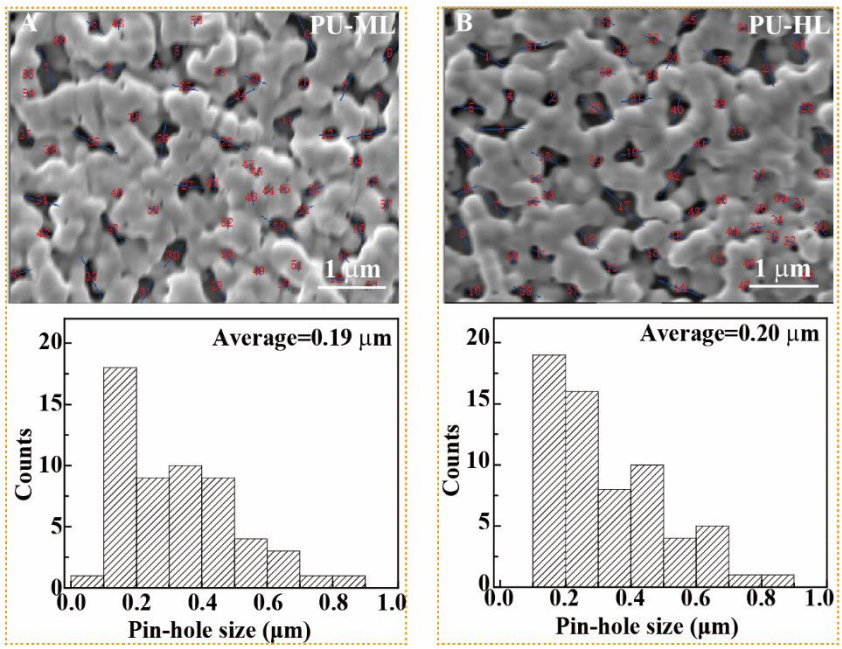

Supplementary Figure 3. The surface morphology and pore size distribution of (A) PU-ML and (B) PU-HL precursor film.

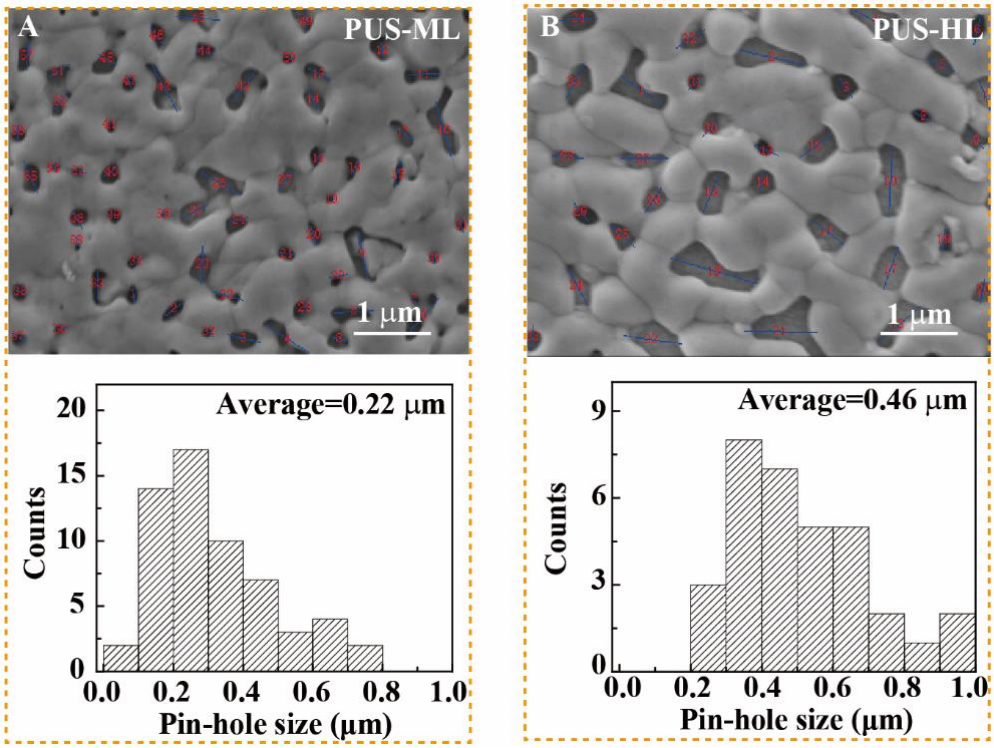

Supplementary Figure 4. The surface morphology and pore size distribution of (A) PUS-ML and (B) PUS-HL precursor film.

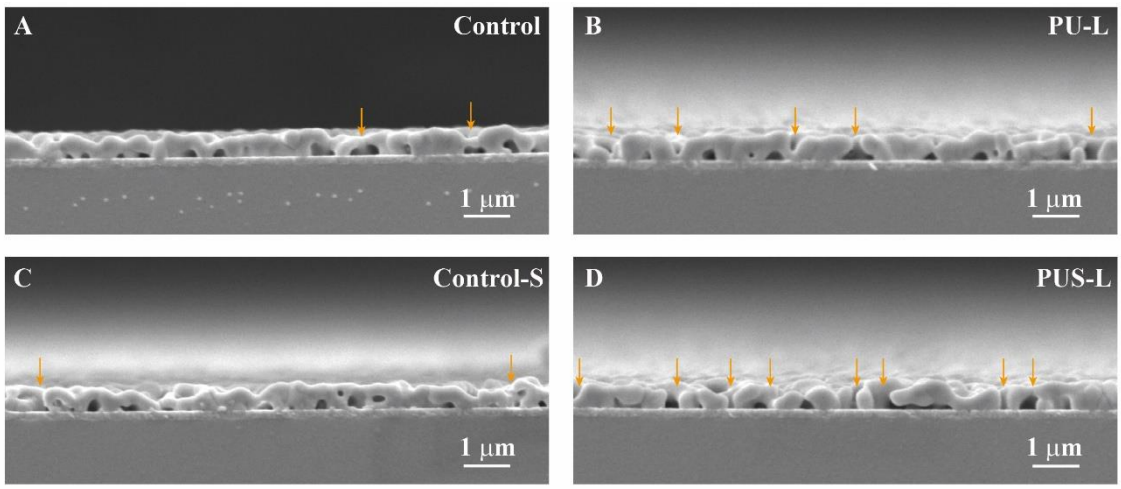

Supplementary Figure 5. Cross-sectional SEM images of the (A) control, (B) PU-L, (C) control-S, and (D) PUS-L $Pb(NO_3)_2$ precursor films. The arrows indicate representative internal pores or voids within the precursor layers.

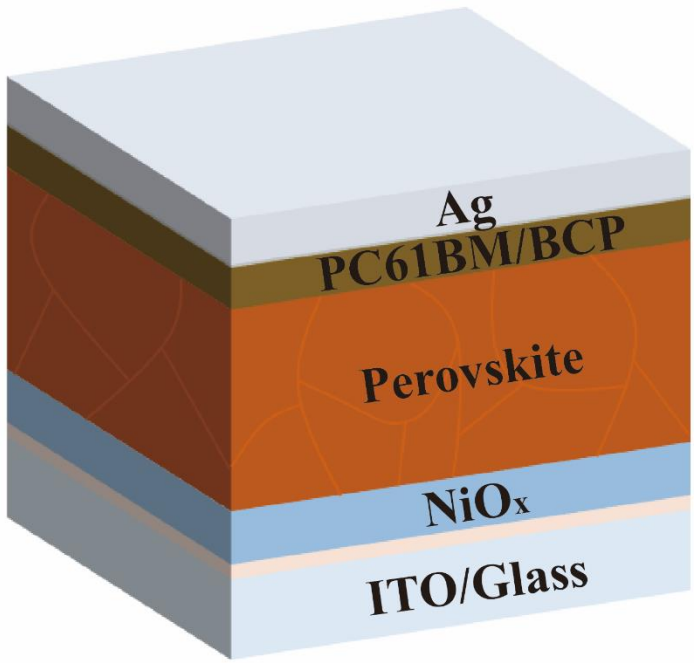

Supplementary Figure 6. Schematic diagram of the PIW-PSCs device structure.

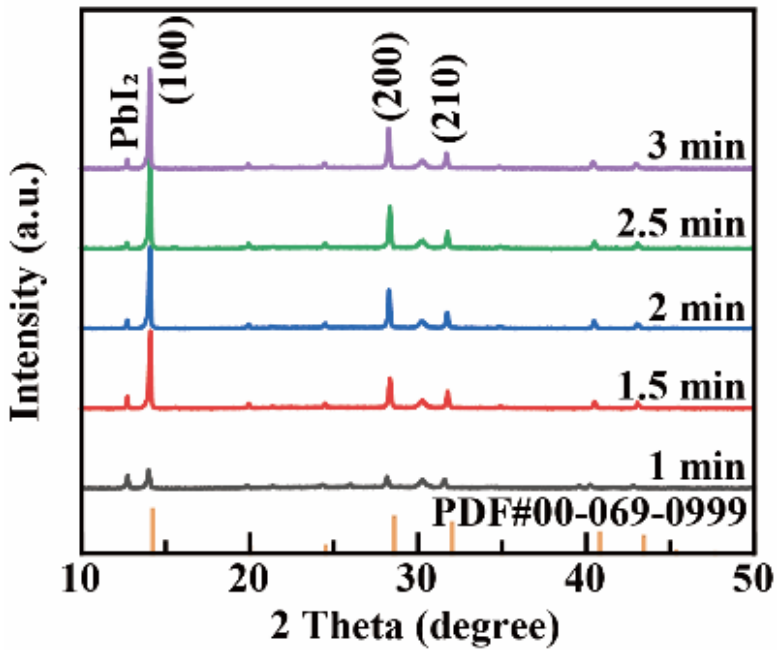

Supplementary Figure 7. XRD patterns of perovskite films prepared using control precursor films incubated in the OAS solution for different durations.

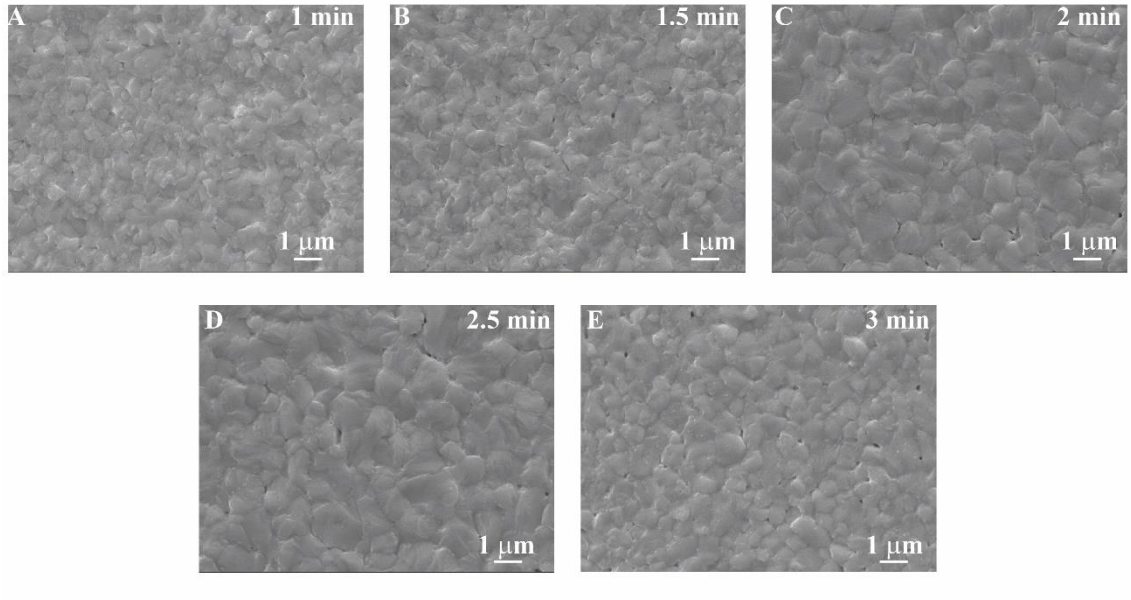

Supplementary Figure 8. Surface SEM images of perovskite films prepared using control precursor films incubated in the OAS solution at 50 °C for (A) 1.0 min, (B) 1.5 min, (C) 2.0 min, (D) 2.5 min, and (E) 3.0 min.

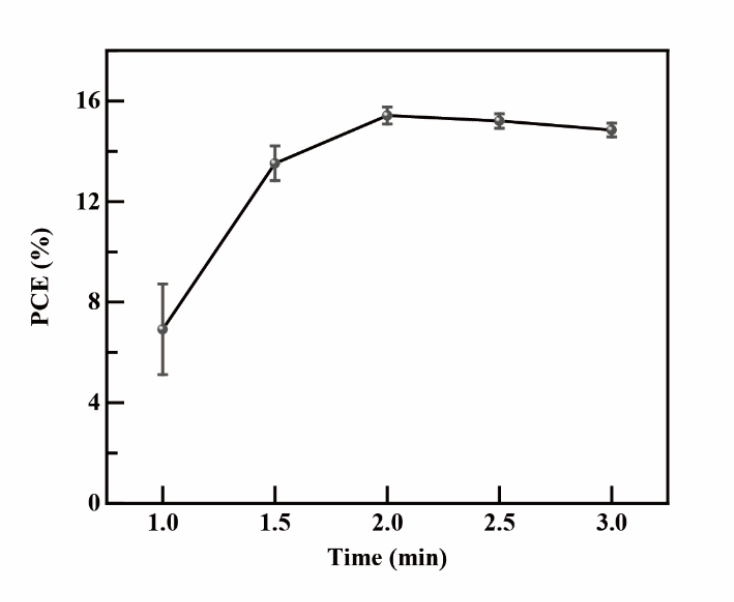

Supplementary Figure 9. PCEs of devices prepared using control precursor films incubated in the OAS solution for different durations. Error bars represent the standard deviation obtained from 11 sub-cells (n=11) for each incubation time.

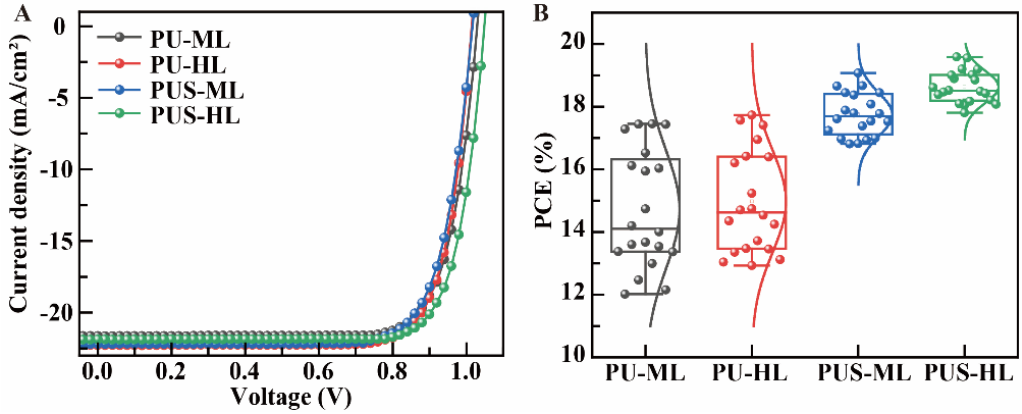

Supplementary Figure 10. (A) J-V characteristic curves of devices. (B) Box plots of PCE based on 20 sub-cells for each sample (n=20).

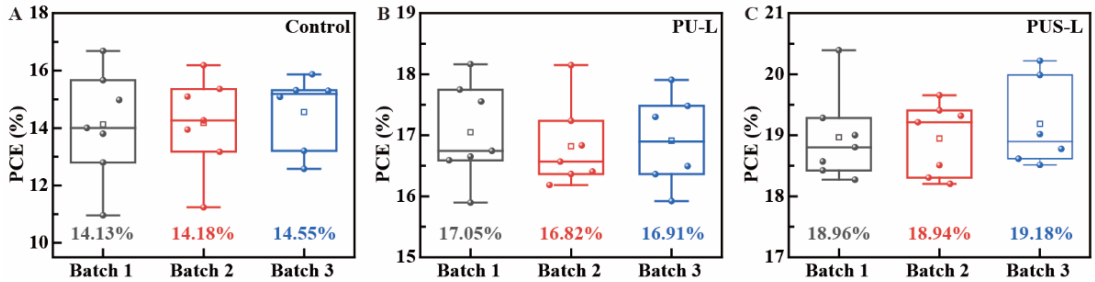

Supplementary Figure 11. Batch-to-batch reproducibility of the photovoltaic performance of (A) control, (B) PU-L, and (C) PUS-L devices fabricated in three independent batches on different days. Individual symbols represent separate sub-cells, and the box plots show the PCE distributions within each fabrication batch. The values below each box represent the mean PCE of the corresponding batch. The numbers of sub-cells in Batches 1, 2, and 3 were n=7, 7, and 6, respectively.

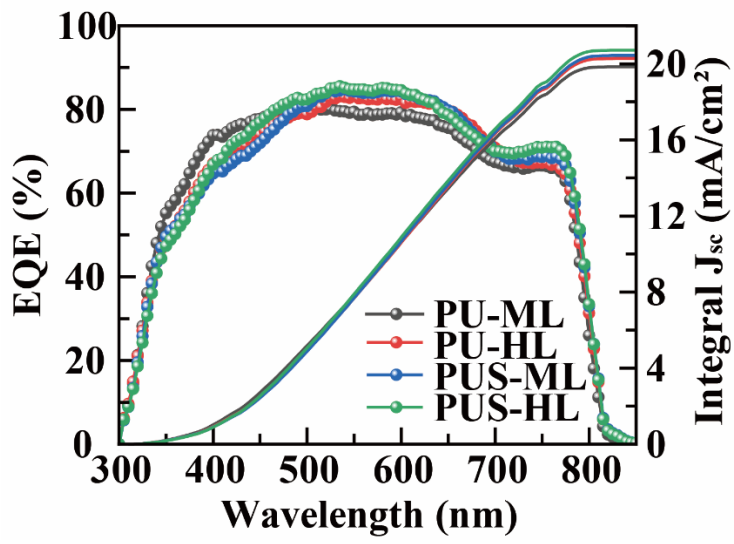

Supplementary Figure 12. EQE spectra and corresponding integrated current densities of representative devices.

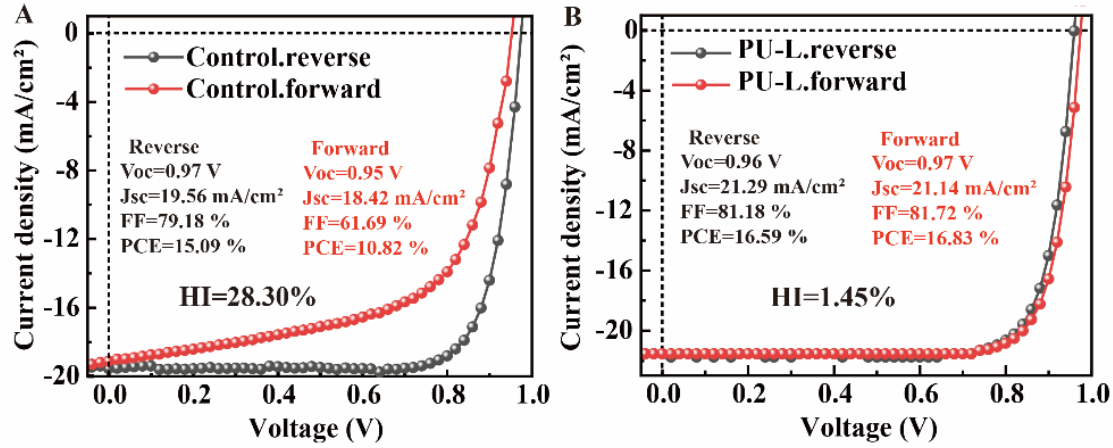

Supplementary Figure 13. The J-V curves of (A) control and (B) PU-L devices under different scan directions. The hysteresis index (HI) is calculated using:[1]

$$HI = \left|\frac{PCE_{reverse} - PCE_{forward}}{PCE_{reverse}}\right| \qquad \text{S1}$$

where $PCE_{forward}$ is the PCE value based on forward scan; $PCE_{reverse}$ is the PCE value based on reverse scan.

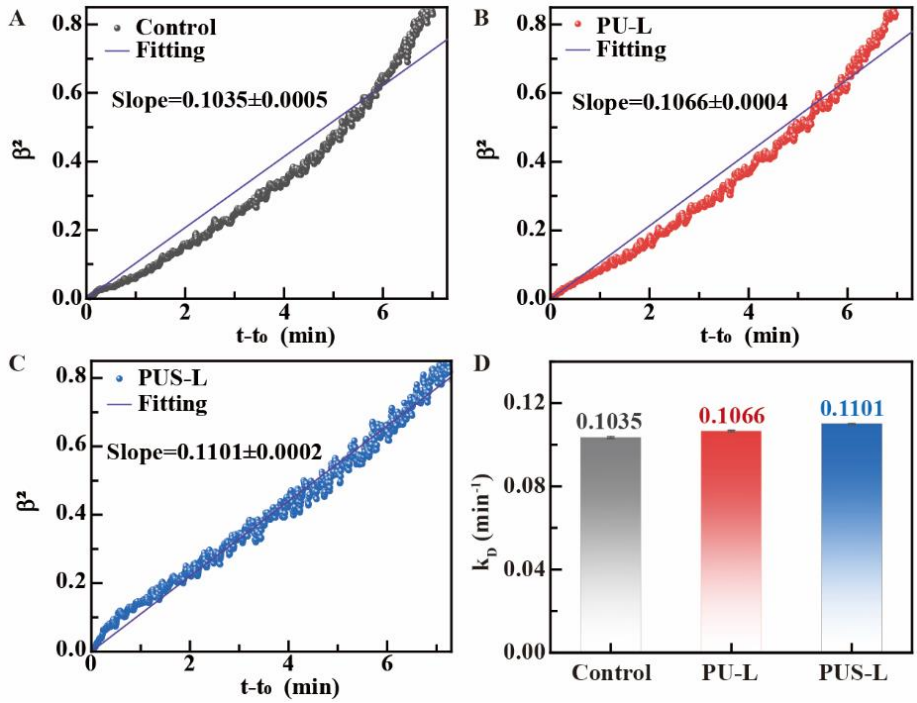

Supplementary Figure 14. D1 diffusion analysis of the late-stage perovskite conversion. Linear plots of β^2 versus $t\text{-}t_0$ for the (A) control, (B) PU-L, and (C) PUS-L films, respectively, where $\beta=[\alpha(t)-\alpha(t_0)]/[1-\alpha(t_0)]$, with $t_0\approx10$ s. The solid lines represent linear fits according to $\beta^2=k_D(t-t_0)$. (D) Apparent diffusion-controlled rate parameter k_D obtained from the corresponding fits. Error bars represent the standard errors of the fitted slopes obtained from linear regression of the individual kinetic traces.

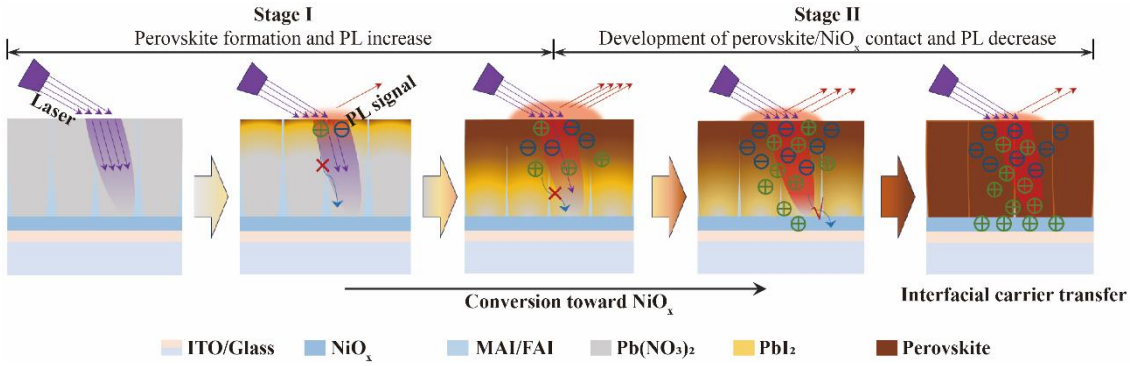

Supplementary Figure 15. Schematic illustration of the proposed PL evolution during the OAS-induced conversion of the $Pb(NO_3)_2$-based precursor film. The initial PL increase accompanies the progressive formation of emissive perovskite. As the conversion proceeds toward the underlying NiO_x layer, perovskite/NiO_x contact is progressively established, and interfacial carrier-transfer and recombination processes may contribute to the subsequent PL decrease.

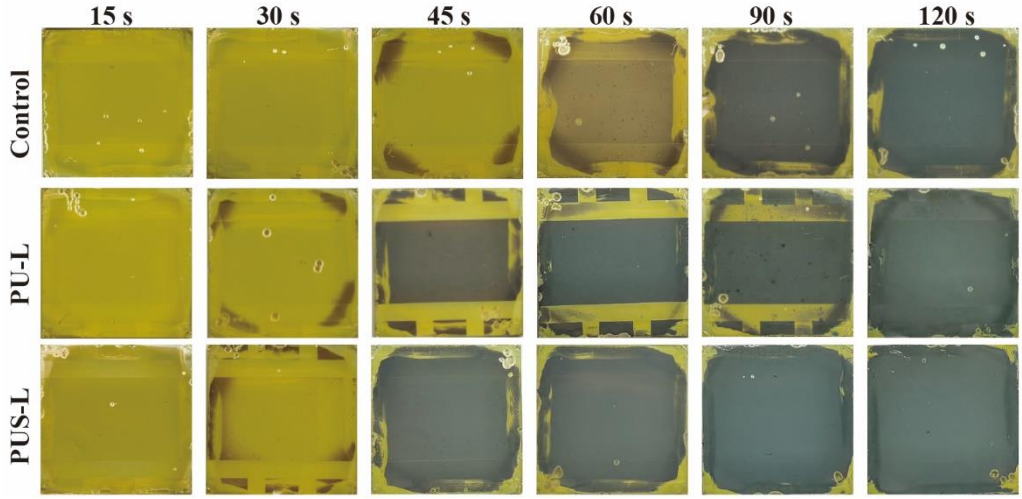

Supplementary Figure 16. Digital photographs of the continuous conversion process of control, PU-L, and PUS-L.

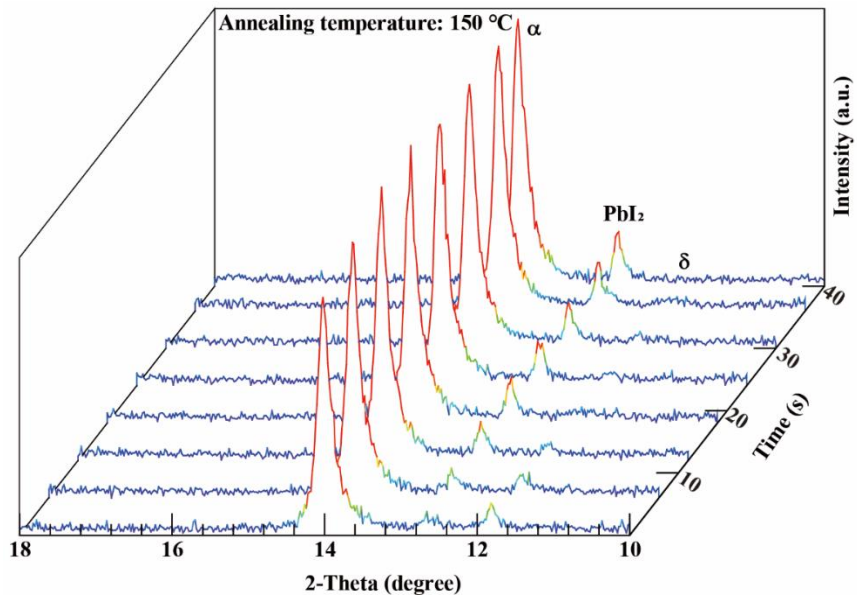

Supplementary Figure 17. Time-dependent XRD patterns of the same perovskite film during annealing at 150 °C. The film was annealed in successive 6 s intervals and characterized by XRD after each interval until the δ-$FAPbI_3$ diffraction disappeared.

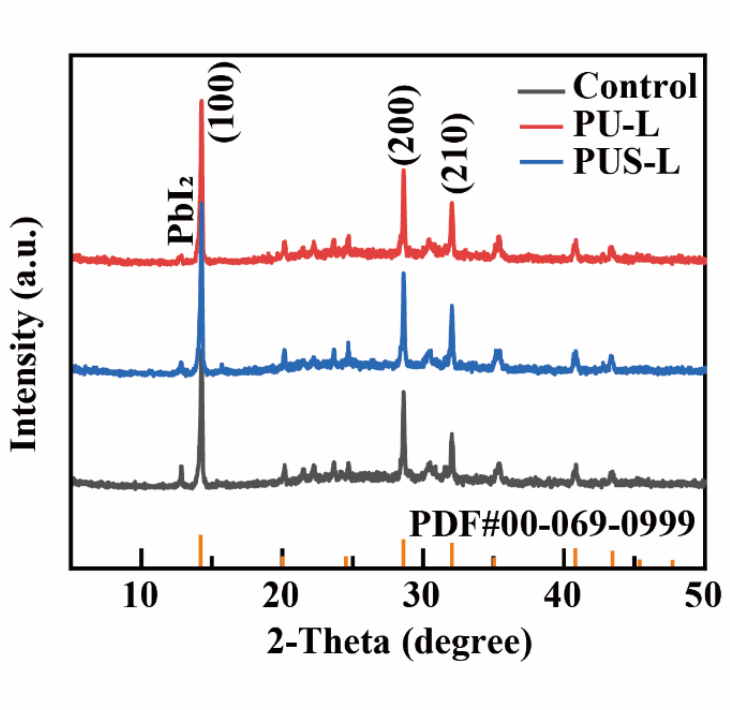

Supplementary Figure 18. The XRD patterns of perovskite films.

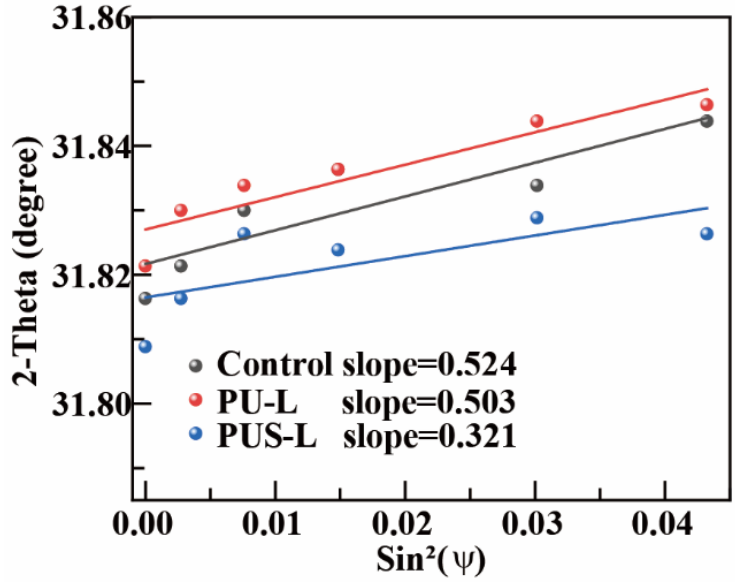

Supplementary Figure 19. Linear fits of 2θ as a function of $\sin^2\psi$ for the (210) reflection of the control, PU-L, and PUS-L perovskite films.

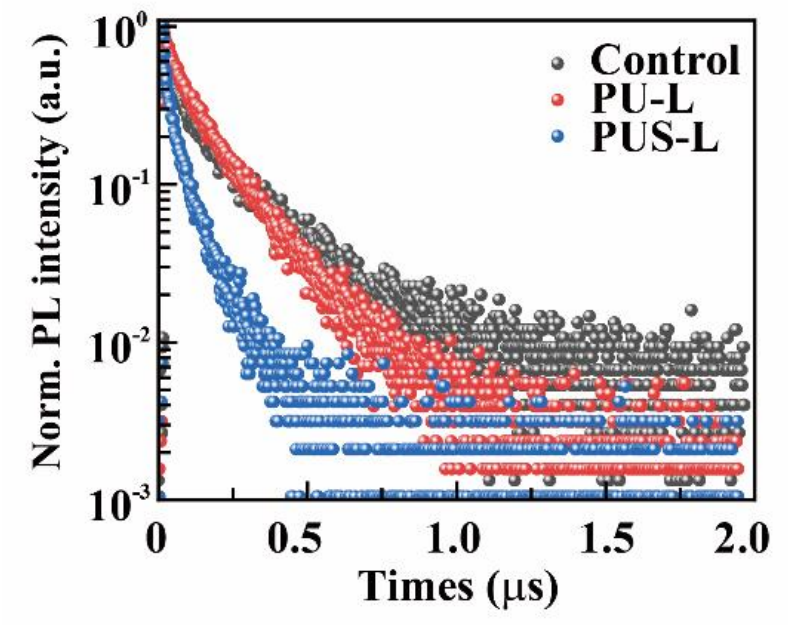

Supplementary Figure 20. TRPL decay curves of the control, PU-L, and PUS-L perovskite films deposited on quartz/NiO_x substrates.

Supplementary Table 1. Photovoltaic performance of control devices prepared using different OAS incubation times at 50 °C

Time (min)	V_{oc} (V)	J_{sc} (mA/cm^2)	FF (%)	PCE (%)
1	0.91±0.09 (1.04)	13.54±1.00 (14.06)	55.61±9.45 (66.11)	6.92±1.80 (9.67)
1.5	1.01±0.02 (1.05)	17.12±0.45 (17.07)	77.87±2.54 (80.96)	13.52±0.69 (14.48)
2	1.06±0.01 (1.06)	17.66±0.42 (18.13)	82.04±0.96 (82.28)	15.42±0.34 (15.84)
2.5	1.06±0.01 (1.06)	17.40±0.38 (17.98)	82.35±1.09 (82.21)	15.20±0.29 (15.70)
3	1.06±0.01 (1.07)	17.41±0.42 (17.83)	80.69±1.05 (80.96)	14.84±0.27 (15.47)

Values are presented as mean±standard deviation (n=11); values in parentheses correspond to the best-performing devices.

Supplementary Table 2. Device performance of PIW-PSCs

Sample	V_{oc} (V)	J_{sc} (mA/cm^2)	FF (%)	PCE (%)
PU-ML	1.01±0.03 (1.03)	19.61±1.16 (21.58)	73.91±5.97 (78.52)	14.72±1.88 (17.45)
PU-HL	1.02±0.02 (1.01)	20.31±1.08 (22.23)	72.32±7.03 (78.61)	14.98±1.64 (17.73)
PUS-ML	1.06±0.02 (1.09)	21.05±0.86 (22.19)	79.33±1.34 (78.87)	17.75±0.69 (19.07)
PUS-HL	1.07±0.01 (1.08)	21.85±0.65 (23.04)	79.75±1.11 (78.75)	18.63±0.51 (19.59)

Values are presented as mean±standard deviation (n=20); values in parentheses correspond to the best-performing devices.

Supplementary Table 3. Comparison of reported photovoltaic performance of PIW-PSCs

Structure	V_{oc} (V)	J_{sc} (mA/cm^2)	FF (%)	PCE (%)	Ref.
Glass/FTO/PEDOT:PSS/Perovskite/PCBM/Au	0.78	8.19	40	2.53	[2]
Glass/ITO/PEDOT:PSS/MoO_3/Perovskite/PCBM/Al	0.86	13.33	56	6.46	[3]
Glass/ITO/PEDOT:PSS/Perovskite/PCBM/BCP/Ag	1.04	19.01	82.26	16.20	[4]
Glass/FTO/NiO_x/Perovskite/PCBM/BCP/Ag	1.03	22.58	79.22	18.34	[5]
Glass/ITO/NiO_x/Perovskite/PCBM/BCP/Ag	1.08	23.33	80.91	20.39	**This work**

Supplementary Table 4. Kinetic fitting parameters for the perovskite conversion measured at 50 °C

Sample	k (min^{-1})	n	R^2_{Avrami}	k_D (min^{-1})	R^2_{D1}
Control	0.624±0.008	0.456±0.006	0.90817	0.1035±0.0005	0.97731
PU-L	1.105±0.018	0.368±0.004	0.91061	0.1066±0.0004	0.98711
PUS-L	1.443±0.022	0.349±0.003	0.94139	0.1101±0.0002	0.99682

The conversion fraction (α) was derived from the time-dependent absorbance at 700 nm. The complete conversion traces were fitted by nonlinear least-squares regression using the Avrami-type expression,

$$\alpha(t) = 1 - \exp\left[-(kt)^n\right]$$

where k is the apparent conversion-rate parameter and n is the Avrami exponent. To evaluate the diffusion contribution to the slower conversion regime, the post-initial conversion was additionally analyzed using the one-dimensional diffusion (D1) relation,

$$\beta = \frac{\alpha(t) - \alpha(t_0)}{1 - \alpha(t_0)}$$

$$\beta^2 = k_D(t - t_0)$$

where β is the normalized conversion fraction, t_0 is the reference time at the beginning of the slower conversion region, and k_D is the apparent diffusion-controlled rate parameter. The measured data point nearest to approximately 10 s was used as t_0 for each sample. Values following "±" represent the standard errors obtained from regression of the individual kinetic traces. R^2_{Avrami} and R^2_{D1} is provided as an indicator of the goodness of fit. As the kinetic measurements were conducted at a single incubation temperature of 50 °C, no Arrhenius activation energy was calculated.

Supplementary Table 5. Fitting parameters of the TRPL decay curves for the control, PU-L, and PUS-L perovskite films deposited on quartz/NiO_x substrates

Sample	τ_1 (ns)	A_1 (%)	τ_2 (ns)	A_2 (%)	τ_{ave} (ns)
Control	11.59	0.54	231.88	0.46	219.67
PU-L	12.49	0.49	175.62	0.51	164.19
PUS-L	6.18	0.61	62.24	0.39	54.70

The PL decay curves are fitted by a bi-exponential decay function as[6]

$$Y = A_1 \exp\left(\frac{-t}{\tau_1}\right) + A_2 \exp\left(\frac{-t}{\tau_2}\right) \qquad \text{S2}$$

where A_1 and A_2 are the relative amplitudes; τ_1 and τ_2 are the lifetime values for the fast and slow decay, respectively.

Supplementary Table 6. EIS fitting parameters of PSCs

Sample	R_s (Ω)	R_{tr} (kΩ)	R_{rec} (kΩ)
Control	19.40	11.49	122.67
PU-L	26.36	6.93	157.10
PUS-L	27.77	14.36	246.20

R_s represents the series resistance arising from the electrodes, electrical contacts, and other ohmic contributions. R_{tr} is assigned to the high-frequency transport-related or interfacial charge-transfer process, whereas R_{rec} describes the resistance associated with carrier recombination. The fitted parameters were interpreted together with the transient photocurrent and transient photovoltage results because electronic transport, recombination, and ionic relaxation may contribute concurrently to the impedance response.[7]

REFERENCES

1. Habisreutinger, S.N.; Noel, N.K.; Snaith, H.J. Hysteresis index: a figure without merit for quantifying hysteresis in perovskite solar cells. *ACS Energy Lett.* **2018**, *3*, 2472-2476, DOI:10.1021/acsenergylett.8b01627.
2. Pothiklang, C.; Hongsith, K.; Ruankham, P.; SupabChoopun. Synthesis of perovskite film by using lead nitrate as precursor for perovskite solar cell applications. *Mater. Today Proc.* **2019**, *17*, 1224-1230, DOI:10.1016/j.matpr.2019.06.002.
3. Irshad, Z.; Adnan, M.; Lee, J.K. Efficient planar heterojunction inverted perovskite solar cells with perovskite materials deposited using an aqueous non-halide lead precursor. *Bull. Korean Chem. Soc.* **2020**, *41*, 937-942, DOI:10.1002/bkcs.12092.
4. Dai, Z.; He, X.; Li, M.; Zhu, H.; Kannan, R.R.; Xu, C.; You, J.; Ma, H.; Zheng, N.; Song, Q. Thermally assisted energy barrier engineering for high-performance planar inverted perovskite solar cells processed with aqueous green solvents. *J. Alloys Compd.* **2025**, *1035*, 181462, DOI:10.1016/j.jallcom.2025.181462.
5. Dai, Z.; He, X.; Jiang, Z.; Zhu, H.; Jiang, H.; Zhang, Q.; Peng, Z.; Tan, Y.; Elseman, A.M.; Song, Q. How to construct efficient planar inverted aqueous-based perovskite solar cells using NiO_x hole transport layers? *ACS Sustain. Chem. Eng.* **2025**, *13*, 22005-22015, DOI:10.1021/acssuschemeng.5c08996.
6. Yuan, Y.; Yan, G.; Dreessen, C.; Kirchartz, T. Understanding Power-Law Photoluminescence Decays and Bimolecular Recombination in Lead-Halide Perovskites. *Adv. Energy Mater.* **2024**, *15*, 2403279, DOI:10.1002/aenm.202403279.
7. Betancur, P.F.; Solis, O.E.; Abargues, R.; Ripolles, T.S.; Boix, P.P. Recombination resistance identification through current-voltage curve reconstruction in perovskite solar cells. *Phys. Chem. Chem. Phys.* **2024**, *26*, 29904-29912, DOI:10.1039/d4cp04143g.